Available online at www.sciencedirect.com
ScienceDirect
Dynamics of Atmospheres and Oceans
44 (2007) 1–28
dynamics of atmospheres and oceans
www.elsevier.com/locate/dynatmoce

# Internal boundary layers in a well-mixed equatorial atmosphere/ocean

Uwe Harlander*, Leo R.M. Maas

*Netherlands Institute for Sea Research, P.O. Box 59, 1790 AB Texel, The Netherlands*

Received 14 May 2007; accepted 25 May 2007
Available online 13 June 2007

**Abstract**

It is known that a non-viscous homogeneous fluid confined to a rotating spherical shell neither possesses a discrete eigenvalue spectrum nor smooth eigenmodes. Mathematically, the motion of a fluid in a rotating spherical shell is governed by a hyperbolic boundary value problem. Generic features of such problems are singularities in the flow field, referred to as internal boundary layers. Physically, these singularities correspond to wave attractors, that are regions to which all inertial waves in the fluid are inevitably drawn. This focusing results from multiple reflections of the inertial waves at boundaries. Therefore, internal boundary layers typically occur for enclosed fluids.

The model studied here is a certain approximation to the equatorial region of a rotating spherical shell. It describes the structure of slow, zonally symmetric inertial waves of a homogeneous fluid in the neighborhood of the equator, enclosed between a flat lower and upper boundary. Exact solutions, computed by a method that can handle hyperbolic boundary value problems, are discussed. Solutions for different frequencies show inertial boundary layers, corresponding with internal wave attractors. The boundary layers consist of alternating shear layers aligned along the wave attractor. They show a self-similar pattern that becomes infinitely thin at the position of the attractor.

In addition to the results discussed, the paper is intended to introduce the concept of internal boundary layers and wave attractors to the broader meteorologic and oceanographic community. As in almost all theoretical studies of geophysical flows, strong model simplifications are required to find solutions analytically. Nevertheless, it is believed that this approach is useful to highlight fundamental properties of equatorial internal boundary layers that might be important for atmosphere and ocean.


*Keywords:* Internal boundary layers; Inertial waves; Equatorial trapped waves; Hyperbolic boundary value problems

* Correspondence address: Lehrstuhl fuer Aerodynamik und Stroemungslehre, BTU-Cottbus, Siemens-Halske_Ring 14, 03046 Cottbus, Germany. Tel.: +31 222 369407; fax: +31 222 319674.
*E-mail address:* harland@nioz.nl (U. Harlander).

0377-0265/$ – see front matter © 2007 Elsevier B.V. All rights reserved.
doi:10.1016/j.dynatmoce.2007.05.001

## 1. Introduction

There are phenomena in the ocean and the atmosphere where multiple wave reflections between surface and bottom are important. The formation of internal tides in slope-shelf regions is an example from oceanography (Vlasenko et al., 2005). For the atmosphere, the most prominent example might be the formation of mountain lee waves. Under certain conditions (Pichler, 1986), a standing resonance wave pattern emerges in the lee of mountains where the wave energy travels up and down between the surface and an internal, reflective sheet in the upper part of the troposphere. Regular patterns of trapped waves are observed by satellites and they can stretch across hundreds of kilometers. Another phenomenon, caused by multiple boundary reflections of internal waves, is the development of internal boundary layers, defined as boundary detached singularities in the velocity field. This is the feature we will focus on in the present paper.

Internal boundary layers are typical for solutions of hyperbolic boundary value problems. Such problems are natural in the context of internal waves in confined fluids and therefore they are much less exotic as they might appear on a first glance. For example, the problem of finding eigensolutions in a rotating spherical shell, filled with a homogeneous or a stratified fluid can be reduced to a hyperbolic boundary value problem. This implies that internal boundary layers are present in one of the most fundamental problems of geophysical fluid dynamics. A strongly simplified version of the spherical shell problem was studied over 40 years ago by Stern (1963). He investigated trapped, zonally symmetric waves in a homogeneous fluid on the equatorial beta plane. Although strongly simplified and therefore limited, the hyperbolic boundary value problem of Stern contains almost all the interesting and perhaps unexpected features of the original spherical shell model. Most important, in contrast to the spherical shell it can be solved exactly. This opens the possibility for an unclouded view on the structure of the internal boundary layers.

Bretherton (1964) realized that the trapped solutions discussed by Stern correspond to periodic orbits of the equation's characteristics.[1] Somewhat later, Israeli (1972) and Stewartson (1972) noted that these orbits are actually limit cycles that attract waves. They showed that singularities in the velocity field (in fact overlooked by Stern) can be expected. Since then, wave attractors have been discussed for internal gravity waves (no rotation), inertial waves (no stratification), inertio-gravity waves (stratification and rotation), for plane, annular, and spherical geometry, by means of theoretical and numerical models, and by laboratory experiments (Maas and Lam, 1995; Kerswell, 1995; Hollerbach and Kerswell, 1995; Maas et al., 1997; Fotheringham and Hollerbach, 1998; Tilgner, 1999; Maas, 2001; Manders and Maas, 2003); an up-to-date review is given by Maas (2005). They are discussed in different geophysical contexts, for example in an astrophysical (Dintrans et al., 1999; Rieutord et al., 2001; Ogilvie and Lin, 2004), and an oceanographical context (Stewartson and Walton, 1976). Therefore, it is justified to say that the existence of wave attractors (and related internal boundary layers) in confined oscillating fluids is well known. However, their relevance for processes in the earth's atmosphere is not clear yet. Stronger, to our knowledge they are not even discussed in the more recent meteorological literature. This appears to be unjustified in view of the fact that, as pointed out in Appendix A, the vertically propagating wave energy can be trapped not only in the ocean but also in the earth's troposphere.

Recently, Rieutord et al. (2002) numerically studied the oscillations of a rotating viscous fluid in the equatorial region of a thin spherical shell. They concentrated on the eigenvalue spectrum

[1] In general, characteristics and short wave energy rays of linear second order partial differential equations differ. However, for Stern's equation it can be shown that there is an exact correspondence between characteristics and energy rays (Harlander and Maas, 2006).

when viscosity becomes very small. In the present paper, in contrast, we discuss exact non-viscous solutions of Stern's purely hyperbolic boundary value problem which does not possess a discrete eigenvalue spectrum. Such solutions cannot be computed with traditional numerical techniques but came into reach with the help of a solution technique that can handle ill-posed hyperbolic boundary value problems. The method, developed by Maas and Lam (1995), is referred to as characteristic web method. Briefly speaking, the method first gives the boundary regions (called fundamental intervals) where data can be specified in order to make the problem well-posed, and second, it gives the solutions in the interior by mapping the characteristics of the problem into the fundamental intervals. The solutions illustrate the occurrence of internal boundary layers which might have a prominent effect on the equatorial dynamics. The role that internal boundary layers play for equatorial waves might be comparable to the role that critical layers play for Rossby waves: in both types of layers, wave energy density blows up and waves can break. The related wave momentum flux can drive observed zonal mean flows (Maas, 2001), and fluid can be mixed, e.g. across the ocean's thermocline or from the troposphere into the stratosphere.

For equatorial tropospheric motion, two distinctly different flow regimes can be identified (Klein, 2003). For the first one, labeled 'weak temperature gradient' regime, vertical motions are suppressed if energy source terms are neglected (Charney, 1963; Majda and Klein, 2003). In this situation, discussed first by Charney for large-scale equatorial motions, the Intertropical Convergence Zone (and possibly other convectively active regions) is considered as an internal boundary layer, not resolved by the model. In the other regime, the equatorial troposphere is considered to be convectively mixed, thus it involves nearly neutral stratification. As discussed first by Ogura and Phillips (1962), in this regime air parcels can move freely in the vertical direction. In the present paper the latter situation is considered. That is we assume a model atmosphere that is neutral in the troposphere but has a large stratification in the tropopause. In that limit, upward propagating inertial waves of all frequencies in the range $0 < \sigma < 2\Omega$ (where $\Omega$ is the earth's angular velocity) are reflected at the troposphere–tropopause interface (see discussion in Appendix B).

Recently, Maas and Harlander (2007) discussed inertial wave attractors of three different models of equatorial motion, including Stern's model. That paper demonstrates that for general geometries of the upper and lower boundary, wave attractors exist for certain frequency bands. Adding stratification to Stern's model gives rise to lateral turning surfaces which lead to a significant broadening of the wave attractor frequency bands and opens the possibility for bottom trapped waves. In the present paper, in contrast, we discuss exact solutions of Stern's model systematically and we explain in detail the characteristic web technique. There are noteworthy differences between the non-viscous solutions of a fully closed convex domain[2] discussed by Maas and Lam (1995), the viscous solutions of a fully enclosed concave domain studied by Rieutord et al. (2002), and the non-viscous solutions of a semi-enclosed concave equatorial region focused on in the present paper. Moreover, we check to see whether the internal boundary layers could be relevant for well-mixed equatorial atmospheres. We believe that such layers deserve attention in the meteorological as well as the oceanographical community.

The paper is organized as follows. In Section 2 we derive Stern's equation. In Section 3 we discuss solutions of Stern's equation for different frequencies. In Section 4 we demonstrate that the existence of internal shear layers is not restricted to Stern's model but can be found also in models including stratification and a weak vertical shear. In Section 5 we give conclusions. Two

[2] A domain is called convex, if it contains all line segments connecting any pair of its interior points.

appendices are added. In Appendix A we describe the characteristic web method used to solve Stern's equation. Finally, in Appendix B we estimate reflection and transmission coefficients for internal waves propagating towards the tropopause.

## 2. Model and method of solution

In Section 2.1 we show how the Boussinesq equations for the equatorial beta plane can be reduced to a single streamfunction equation, describing the wave motion in the meridional plane of the equatorial region (Stern, 1963). Introducing characteristic coordinates in Section 2.2, Stern's equation can be transformed to the classical wave equation. Due to their separability (in terms of characteristics), it can be solved by the characteristic web method (Maas and Lam, 1995). This method is explained in detail in Section 2.3.

### 2.1. Model

We start by considering the Boussinesq equations on the equatorial beta plane. In deviation from standard models we keep also terms related to the horizontal components of the Coriolis force, the so called non-traditional terms. Such terms, usually neglected in ocean and meteorology applications, gain importance in tropical regions and there is scepticism in the literature about the validity of the traditional approximation (Hendershott, 1981; Gerkema and Shrira, 2005). Colin de Verdière and Schopp (1994) showed that if the horizontal scale $L$ is smaller than $(HR)^{1/2}$, where $H$ is the vertical scale of motion and $R$ is the earth radius, then equatorial dynamics must include the effect of the horizontal component of the Coriolis force.

The linearized model equations read in dimensional form (for harmonic motions in time):

$$i\sigma^* u^* + 2\Omega w^* - \beta y^* v^* = -p^*_{x^*}, \tag{1}$$

$$i\sigma^* v^* + \beta y^* u^* = -p^*_{y^*}, \tag{2}$$

$$i\sigma^* w^* - 2\Omega u^* = -p^*_{z^*} + b^*, \tag{3}$$

$$i\sigma^* b^* + w^* N^2 = 0, \tag{4}$$

$$u^*_{x^*} + v^*_{y^*} + w^*_{z^*} = 0, \tag{5}$$

where $p^*$ is the pressure perturbation divided by the mean density $\rho_s$, buoyancy $b^* = -g\theta^*/\theta_s$, $g$ the constant of gravity, $\theta_s$ the mean of the potential temperature, $\theta^*$ the perturbation of the potential temperature, $N^2 = -(g/\theta_s)(\mathrm{d}\theta_0/\mathrm{d}z)$ is a constant Brunt–Väisälä frequency, $\theta_0(z)$ the hydrostatic part of the potential temperature, $u^*$, $v^*$, $w^*$ are the zonal ($x^*$), meridional ($y^*$), and vertical ($z^*$) velocity components, $\Omega$ the earth's angular frequency, $\beta = 2\Omega/R$, and, finally, $\sigma^*$ is the frequency of the waves. Note that a super-rotational mean flow can be included in $\Omega$. Then the coordinate system co-rotates with the atmosphere and not with the earth. We are interested here in the zonally symmetric part of the solution. Therefore, we integrate the above equations over $x$ and apply zonal periodicity as 'boundary condition.' Then all terms with zonal derivatives vanish from (1)–(5). Next we introduce typical scales to non-dimensionalize the equations. Following Stern (1963) we use:

$$[y^*, z^*, \sigma^*, u^*, v^*, w^*, p^*] = (Ly, \epsilon Lz, 2\Omega\epsilon\sigma, Uu, Uv, \epsilon Uw, 2\Omega\epsilon LUp), \tag{6}$$

where $\epsilon = L/R \ll 1$. Note that $U$ is the velocity scale of the wave motion and not of a zonal mean flow. Stern considered a homogeneous fluid ($N = 0$). In contrast, here we scale the buoyancy by $b^* = 2\Omega U\epsilon b$ and assume $N^2 \sim (2\Omega\epsilon)^2\sigma$, to obtain the non-dimensional system:

$$i\sigma u + w - yv = 0, \tag{7}$$

$$i\sigma v + yu = -p_y, \tag{8}$$

$$i\epsilon^2\sigma w - u = -p_z + \epsilon b, \tag{9}$$

$$b - i\epsilon w = 0, \tag{10}$$

$$v_y + w_z = 0. \tag{11}$$

By neglecting terms of order $\epsilon$ or smaller, the dynamics reduces to the one of a homogeneous fluid. Introducing a streamfunction in the meridional plane $v = -\psi_z$, $w = \psi_y$, we find from (7)–(11):

$$\psi_{yy} - (\sigma^2 - y^2)\psi_{zz} + 2y\psi_{yz} + \psi_z = 0, \tag{12}$$

which is Stern's equation (Stern, 1963). As boundary conditions we use $\psi = 0$ at $z = 0$ (bottom) and at $z = 1$ (top).

### 2.2. Stern's equation in canonical form

The characteristic curves of (12) are given by the ordinary differential equation:

$$\frac{\mathrm{d}y}{\mathrm{d}z} = \frac{1}{y \pm \sigma}. \tag{13}$$

Details on characteristics for linear second order equations can be found for example in the book by Myint-U (1987) on page 30–34. By integration, (13) gives the characteristic coordinates:

$$\zeta = z - \frac{1}{2}y^2 - \sigma y, \tag{14}$$

$$\eta = z - \frac{1}{2}y^2 + \sigma y. \tag{15}$$

Using the variables:

$$Y = 2(\eta - \zeta) = 4y\sigma, \tag{16}$$

$$Z = 2(\eta + \zeta - \sigma^2) = 2(2z - y^2 - \sigma^2). \tag{17}$$

Eq. (12) is reduced to the (spatial) wave equation (Maas and Harlander, 2007):

$$\psi_{YY} - \psi_{ZZ} = 0. \tag{18}$$

In this frame, characteristics are straight lines with slopes of $\pm 1$. Solutions of (18) are

$$\psi(Y, Z) = f(Y + Z) - g(Y - Z), \tag{19}$$

where $f$ and $g$ are arbitrary functions. Note that the flat earth's surface and the flat upper boundary ($z = 0, 1$) of (12) turn into two displaced parabola in the $Y$–$Z$-frame. Bottom and surface are

given as

$$Z_{\mathrm{b}}(Y) = -2\left(\frac{Y^2}{16\sigma^2} + \sigma^2\right), \tag{20}$$

$$Z_{\mathrm{s}}(Y) = Z_{\mathrm{b}}(Y) + 4. \tag{21}$$

Imposing the boundary conditions $\psi = 0$ at $Z = Z_{\mathrm{s}}, Z_{\mathrm{b}}$ we find that

$$g(Y - Z_{\mathrm{s,b}}) = f(Y + Z_{\mathrm{s,b}}). \tag{22}$$

Let us consider a single point at the boundary where a characteristic, on which a certain $f$-value is constant, is reflected. Obviously, the $g$-value of the reflected characteristic has to be equal to the $f$-value in order to satisfy the boundary condition at the point of reflection. In other words, all characteristics connected via boundary reflections (a characteristic web), carry the same value. Consequently, the $f$-value, corresponding to the initial characteristic is invariant along the whole web. Thus, it is sufficient to specify $f$ in a single point of the web.

### 2.3. Characteristic web method

Let us assume for a moment that there is no upper boundary $Z_{\mathrm{s}}$. In other words, the waves can radiate away from $Z_{\mathrm{b}}$ without any back scatter. Then (18) forms a classical Cauchy problem, i.e. if $\psi$, $\psi_Y$ and $\psi_Z$ are given along $Z_{\mathrm{b}}$, a unique solution exists for any choice of the boundary data. Owing to the boundary conditions, the boundary data are given completely by specifying $f$ along $Z_{\mathrm{b}}$. For any point $P$ above $Z_{\mathrm{b}}$ the solution $\psi(P)$ can easily be found by reading off the $f$-values at the points where the $c^+$ and the $c^-$ characteristics connect $P$ with the boundary $Z_{\mathrm{b}}$ ($c^+$ and $c^-$ denote the characteristics that correspond with a positive and negative slope, respectively).

Coming back to the original problem and introducing a reflective upper boundary $Z_{\mathrm{s}}$, a serious problem occurs. Now, characteristics can be reflected between the two boundaries and, in general, the $f$-values in an arbitrary interval along $Z_{\mathrm{b}}$ cannot be chosen independently from the $f$-values in another interval. Mathematically spoken, (18) with boundary conditions at $Z_{\mathrm{b}}$ or $Z_{\mathrm{s}}$ forms an ill-posed problem and we cannot find solutions if $f$ is given along the whole lower or upper boundary. Maas and Lam (1995) solved this problem by introducing so called fundamental intervals. These intervals can be characterized best by the following property: a characteristic 'launched' from a fundamental interval and followed by subsequent boundary reflections (forming a so called characteristic web) may never intersect with the same or another fundamental interval. Then the data in the fundamental intervals are independent and, by specifying $f$ in the fundamental intervals only, a unique solution can be constructed.

A detailed description how fundamental intervals can be found is given in Appendix A. Moreover, we explain why symmetric/anti-symmetric solutions cannot be expected for an arbitrary choice of data in the fundamental intervals. Finally, we estimate the number of fundamental intervals for different frequencies in Appendix A.

## 3. Results

The characteristic web method, described in detail in Appendix A, will now be used to find solutions of Stern's equation. From the discussion above it is obvious that the boundary data $f$ can be prescribed arbitrarily in the fundamental intervals. If, for instance, $f$ is non-continuous in one of the fundamental intervals, the solution will be non-continuous too. Even continuous data in each

fundamental interval generally give non-continuous solutions. In any case the solution will not be everywhere differentiable, that is the velocity field will show singularities (referred to as internal boundary layers) at limit cycles of the characteristic web (Maas and Lam, 1995). Therefore, it is appropriate to extend the solution space and allow for non-continuous, so called *weak solutions*. Weak solutions are common in the context of nonlinear hyperbolic equations and conservation laws (LeVeque, 2002). In some sense we can say that boundaries can lead to shock-like structures in the velocity field, even for *linear* hyperbolic equations.

### 3.1. Weak solutions

Let $\phi(Y, Z)$ be a set of smooth functions with compact support, that is $\phi$, $\phi_Y$, and $\phi_Z$ go to zero outside some bounded region in the $Y$–$Z$-plane. Now we define $\psi$ such that it has to satisfy:

$$\int_{-\infty}^{+\infty}\int_{-\infty}^{+\infty}(\phi_{YY}-\phi_{ZZ})\psi(Y,Z)\,\mathrm{d}Y\,\mathrm{d}Z=0, \tag{23}$$

in order to be called a weak solution of (18). Note that classical smooth solutions satisfy (23). To show this we multiply (18) with $\phi$ and integrate over space. This gives:

$$\int_{-\infty}^{+\infty}\int_{-\infty}^{+\infty}(\psi_{YY}-\psi_{ZZ})\phi(Y,Z)\,\mathrm{d}Y\,\mathrm{d}Z=0. \tag{24}$$

With the assumption on $\phi$ made above we have:

$$\int_{-\infty}^{+\infty}\psi_{XX}\phi\,\mathrm{d}X=(\phi\psi_X)_{-\infty}^{+\infty}-\int_{-\infty}^{+\infty}\psi_X\phi_X\,\mathrm{d}X, \tag{25}$$

$$\int_{-\infty}^{+\infty}\psi_X\phi_X\,\mathrm{d}X=(\phi_X\psi)_{-\infty}^{+\infty}-\int_{-\infty}^{+\infty}\psi\phi_{XX}\,\mathrm{d}X, \tag{26}$$

where $X$ stands for $Y$ or $Z$. Since the first term on the right-hand side of both equations vanishes we obtain (23) from (24). Thus we have proven that solutions of (18) satisfy (23). However, a nice feature of (23) is that the derivatives are on $\phi$, and no longer on $\psi$. This means that even discontinuous functions $\psi$ can be weak solutions of (18).

Strictly speaking, the solutions that are discussed in the following section are weak solutions of (18). However, for simplicity the adjective ‘weak’ is omitted.

### 3.2. Three solutions of Stern’s equation

The aim of this section is to apply the characteristic web method of Maas and Lam (1995) to Stern’s equation and to discuss the solutions. As it has become clear from the discussion above, the solutions depend on the choice of data in the fundamental intervals. This choice is arbitrary since we have not identified a physical mechanism which requires a particular choice. The situation is similar to classical Cauchy-problems in space and time, where initial conditions can be chosen arbitrarily. Nevertheless, the data in the fundamental intervals are chosen to highlight typical and, from a physical point of view, interesting features. The most interesting aspect, namely the formation of internal boundary layers, is in fact independent of the choice of data in the fundamental intervals.

The frequency has been chosen from frequency intervals where limit cycles of the characteristic web exist (Stewartson, 1972). Maas and Harlander (2007) argue that these continuous frequency

intervals may play a similar role for Stern's hyperbolic boundary value problem as do the discrete sets of eigenvalues for elliptic problems. The shape of the internal boundary layer changes from frequency interval to frequency interval (and sometimes also within a single interval as we will discuss below), but for every interval, internal boundary layers exist. For our choice of frequencies the geometry of the limit cycle is relatively simple. The simpler the limit cycle, the shorter is its total length and the smaller is its number of boundary reflections. Such limit cycles might stand out even when dissipation and scattering are present. Therefore, geometrically simple limit cycles (or internal boundary layers) are believed to be most relevant in practice, and they might be the ones which can be observed in the ocean and the atmosphere. This expectation is supported by laboratory experiments showing that the simplest limit cycles can be observed most easily (Manders and Maas, 2003).

*3.2.1. Solution for frequency $\sigma = 0.9$*

Our task is now to discuss the first example. For $\sigma = 0.9$ we have discussed in detail how the fundamental intervals can be found (see Appendix A). Let us first see which part of the fluid depends on which fundamental interval. Fig. 1a shows the solution corresponding to $f_{I_1} = 1/3$, $f_{I_2} = 1$, and $f_{I_3} = 0$. Moreover, a $c^+$ and a $c^-$ characteristic is displayed in the figure. As can be seen, the two characteristics converge rapidly towards a limit cycle. To interpret the figure a 'color code' is given in Table 1 which has to be read in the following way: a $c^+$ ($c^-$) characteristic 'launched' in the red area will be mapped onto fundamental interval $I_2$ ($I_3$); a $c^+$ ($c^-$) characteristic 'launched' in the purple area will be mapped onto fundamental interval $I_3$ ($I_2$), and so forth. This shows for instance that a change of the data in fundamental interval $I_1$ will have no influence on the solution in the red and purple areas.

An interesting feature which can be seen in Fig. 1a are the two 'beams', radiated away from the equatorial region. From Table 1 we find that wave energy can only be trapped completely in the equatorial regions if we require $f_{I_1} = f_{I_3}$. Then, the contributions from $I_1$ and $I_3$ cancel each other and all blue and green regions turn into light green, standing for $\psi = 0$. Otherwise the waveguide is leaky and wave energy can propagate to the extra-tropics; there the low frequency perturbations might resonate with midlatitude synoptic-scale flows (Majda and Klein, 2003).

In Fig. 1b we display the solution corresponding to data which vary in the fundamental intervals, $f_{I_1} = \sin(\pi[Y - s_{1,2}]/[s_{1,2} - s_{1,1}])$, $f_{I_2} = \sin(\pi[Y - s_{2,2}]/[s_{2,2} - s_{2,1}])$, and $f_{I_3} = 1/8$, where $s_{j,1}$ ($s_{j,2}$) stands for the lower (upper) bound of fundamental interval $j$. In some regions, the solution shows a stripy pattern with alternating up- and downward motions, other regions show a cellular pattern with saddle points in the streamfunction field. Most striking however is the internal boundary layer in which the velocity as well as the velocity shear blows up. To get more insight

Table 1
Colour scheme of Fig. 1a

| | $I_1$ | $I_2$ | $I_3$ |
|---|---|---|---|
| Red | | $c^+$ | $c^-$ |
| Purple | | $c^-$ | $c^+$ |
| Yellow | $c^-$ | $c^+$ | |
| Violet | $c^+$ | $c^-$ | |
| Green | $c^+$ | | $c^-$ |
| Blue | $c^-$ | | $c^+$ |
| Light green | $c^\pm$ | $c^\pm$ | $c^\pm$ |

For details see text.

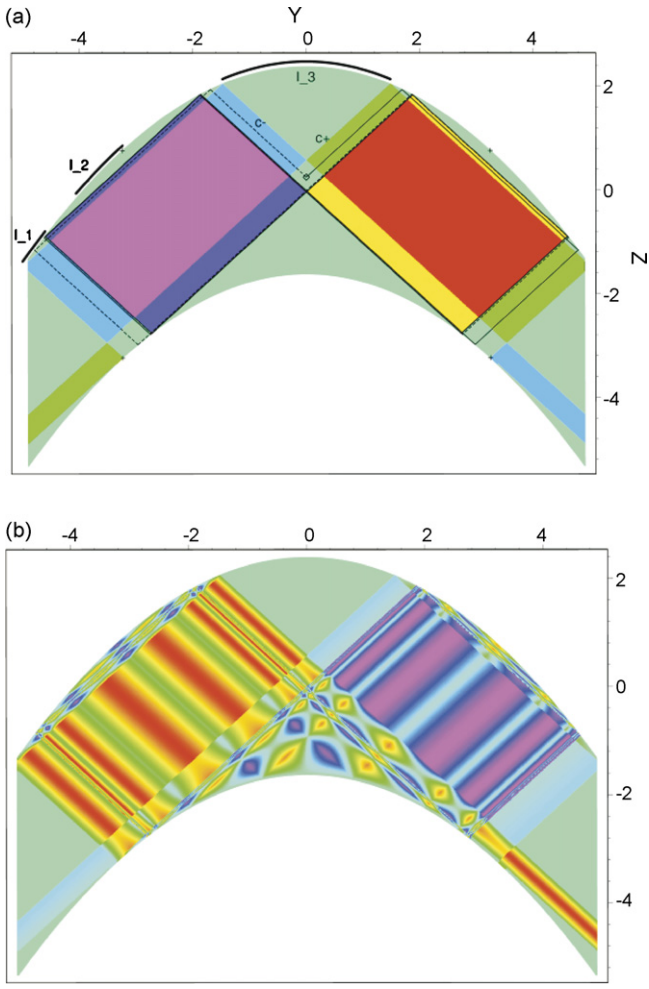


Fig. 1. Two solutions of Stern's equation in terms of streamfunction for $\sigma = 0.9$ in the $Y$–$Z$-frame. The equator is located at $Y = 0$. In (a) $f$ is constant in the fundamental intervals. The fundamental intervals are shown by thick curves above the upper boundary. A $c^+$ (solid line) and a $c^-$ (dashed line) characteristic is launched in the center of the domain. Both characteristics converge towards a limit cycle. In (b) sine functions have been used in the fundamental intervals. For more details see text. The figure b is taken from Maas and Harlander (2007).

into the fine structure of this layer we enlarge a small rectangular region (with upper left corner point (3.9, −1.4) and lower right corner point (4.1, −1.6)), including the boundary layer. Fig. 2a shows a large number of shear layers (note that the color range differs from that in Fig. 1b), perfectly aligned along the limit cycle. Enlarging the inner part of the boundary layer further (Fig. 2b, upper left corner (4.0062, −1.4826), lower right corner (4.01, −1.4865)) uncovers its self-similar nature: more and more shear layers show up, indicating a blow up of velocity. Apart from their physical relevance, the fragile looking filaments of alternating jets in the boundary layer are also appealing from an esthetic point of view.

In practice, dissipative and nonlinear effects control these regions and the fluid is mixed intensively in the internal boundary layer. Physical implications of such processes are discussed by

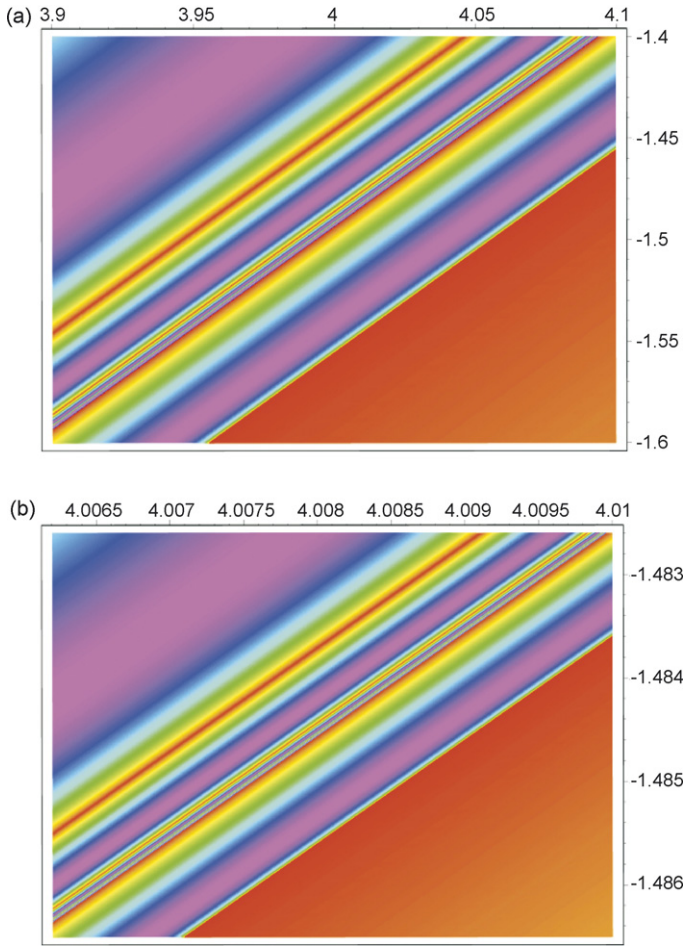


Fig. 2. Zoom in of Fig. 1 b to uncover the fine structure and the self-similarity of the solution in the vicinity of the limit cycle.

Maas (2001). Here we want to point out that laboratory experiments have shown that the efficiency of the mixing is not distributed equally along the limit cycle. Mixing seems to be enhanced where characteristic focusing is strong. For the geometry considered here the two inner points of contact of the limit cycle with the upper boundary correspond with regions of especially strong mixing (Maas, 2001). In our context this could mean that in such regions there is a strong exchange of air between the troposphere and the stratosphere. Such regions could be local sinks of tropospheric moisture.

Note that the self-similar structure of the internal boundary layer neither implies a complicated distribution of fundamental intervals, nor a complicated non-smooth mapping of characteristics into different fundamental intervals. From Fig. 1a and Table 1 we find that all $c^+$ ($c^-$) characteristics to the left of the thinnest layer visible in Fig. 2b are mapped to $I_2$ ($I_3$), and all $c^+$ ($c^-$) characteristics to the right are mapped to $I_1$ ($I_3$). Therefore, in view of the complicated self-similar structure of the boundary layer velocity field, the corresponding characteristic map is strikingly simple.

Table 2
Colour scheme of Fig. 3a

| | $I_1$ | $I_2$ | $I_3$ | $I_4$ |
|---|---|---|---|---|
| Red | | $c^-$ | $c^+$ | |
| Purple | $c^+$ | | $c^-$ | |
| Yellow | $c^-$ | | | $c^+$ |
| Violet | | | $c^-$ | $c^+$ |
| Light blue | | $c^-$ | | $c^+$ |
| Blue | $c^+$ | $c^-$ | | |
| Green | $c^\pm$ | $c^\pm$ | $c^\pm$ | $c^\pm$ |

For details see text.

### 3.2.2. *Solution for frequency* $\sigma = 0.52$

Note that for this frequency, the geometry looks different than for the previous case since the $Y$–$Z$ coordinates depend on $\sigma$. As before we first assume constant $f$ values in the fundamental intervals ($f_{I_1} = 1$, $f_{I_2} = 5/2$, $f_{I_3} = 18/5$, and $f_{I_4} = 4/3$). Together with the 'color code' given in Table 2, Fig. 3a shows which region of the fluid domain is related to which fundamental interval. In addition, the figure shows the characteristic web of a $c^+$ and a $c^-$ characteristic. Interestingly, two independent limit cycles exist. As discussed in Appendix A, we need in total four fundamental intervals (shown as thick curves above the upper boundary in Fig. 3a) to find a unique solution. It should be noted that for $\sigma = 0.5$ the two limit cycles melt into one another to form a single cell, oriented symmetrically with respect to the $Z$-axis. This means that the appearance of the limit cycle can look different within the same continuous frequency band (the bands for $\sigma > 0.8$ are tabulated by Stewartson, 1972, the one for $\sigma < 0.8$ are given in Fig. 2 of Maas and Harlander, 2007).

In Fig. 3b a solution is shown for $f_{I_3} = \sin(3\pi[Y - s_{3,2}]/[s_{3,2} - s_{3,1}])$, $f_{I_1} = f_{I_2} = f_{I_4} = 0$. In contrast to Fig. 1b, functions have been chosen such as to avoid any energy loss due to radiation to extra-tropical latitudes (cf. Table 2). For this choice the red and violet areas of Fig. 3a show a stripy pattern of localized motions, framed by the internal boundary layer.

### 3.2.3. *Solutions for frequency* $\sigma = 0.37$

As can be seen from Fig. 4a, for this frequency the limit cycle looks more complicated than for the other two examples (the limit cycle has 6 cells in contrast to the two cells of the previous cases). However, there exists just one independent limit cycle as was the case for $\sigma = 0.9$, implying three fundamental intervals (see Appendix A). The partitioning of the fluid domain with respect to the three fundamental intervals is shown in Fig. 4a ($f_{I_1} = 1$, $f_{I_2} = 5/2$, and $f_{I_3} = 4/3$) and the corresponding 'color code' is given in Table 3. In Fig. 4b we display the solution belonging to $f_{I_1} = \sin(\pi[Y - s_{1,2}]/[s_{1,2} - s_{1,1}])$, $f_{I_2} = \sin(\pi[Y - s_{2,2}]/[s_{2,2} - s_{2,1}])$, $f_{I_3} = 0$. Viewed from some distance, the solution looks almost like a smooth mode, however, a closer inspection reveals a sharp internal boundary layer coinciding with the limit cycle shown in Fig. 4a. The reason for the 'smooth appearance' of the solution is, first, that the fundamental interval $I_2$ is large and that large parts of the domain are mapped onto it, and second, that the geometry gives rise to a strong focusing of characteristics. Note that in contrast to the solution shown in Fig. 3b the one shown in Fig. 4b is not fully trapped, that is the solution is non-zero outside the equatorial region. Nevertheless, given the large amount of kinetic energy trapped along the internal boundary layer it is justified to say we see a trapped equatorial wave.

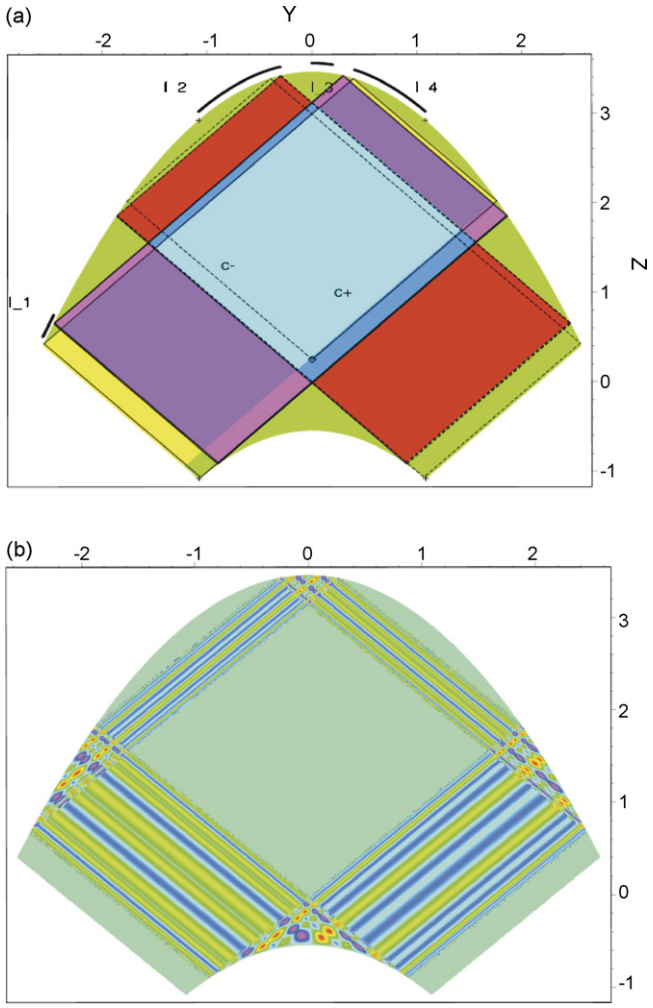


Fig. 3. Two solutions for $\sigma = 0.52$. For more details see text and caption of Fig. 1.

Table 3
Colour scheme of Fig. 4a

| | $I_1$ | $I_2$ | $I_3$ |
|---|---|---|---|
| Red | $c^-$ | $c^+$ | |
| Purple | $c^+$ | $c^-$ | |
| Orange | | $c^+$ | $c^-$ |
| Violet | | $c^-$ | $c^+$ |
| Blue | $c^+$ | | $c^-$ |
| Green | $c^-$ | | $c^+$ |
| Light green | $c^\pm$ | $c^\pm$ | $c^\pm$ |

For details seetext.

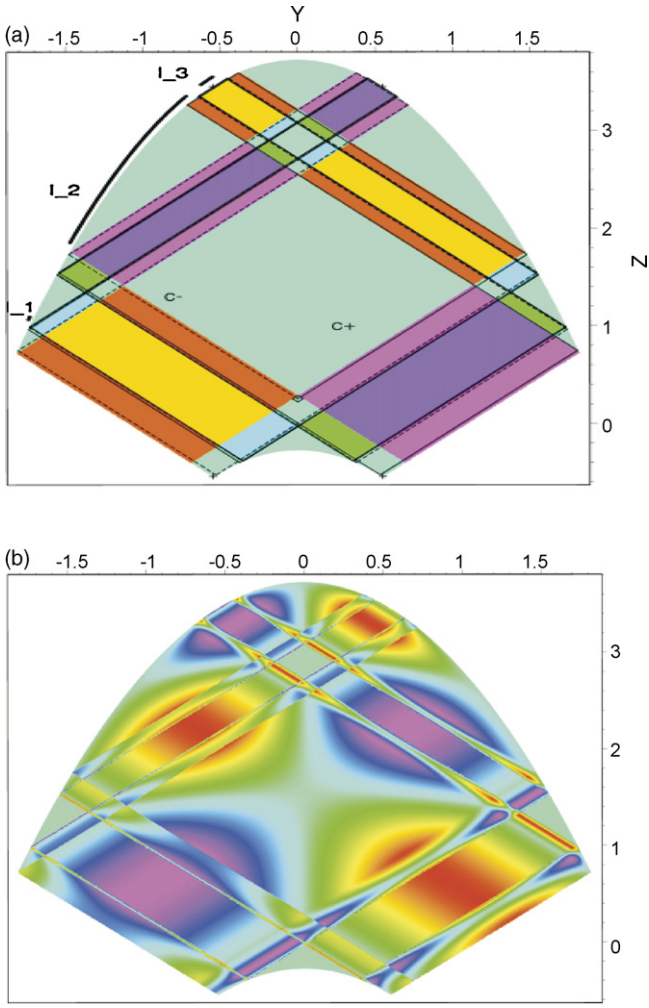


Fig. 4. Two solutions for $\sigma = 0.37$. For more details see text and caption of Fig. 1.

In summary we can say that the examples presented cover several interesting new features deserving attention in the meteorological as well as the oceanographic community. Most important, of course, is the fact that smooth solutions cannot be found and that internal boundary layers are a generic feature of Stern's model describing trapped zonally symmetric equatorial waves.

## 4. Physical validity of the solutions

In this section we discuss scaling variants of (1)–(5) leading to three different equations for the meridional streamfunction. We show that a conventional model that assumes stratification and neglects non-traditional Coriolis terms also shows wave attractors. Using numerical solutions we demonstrate that even a general model including all terms of (1)–(5) shows localized solutions similar to the ones of Stern's model. Therefore, it appears that the validity of the solutions discussed in Section 3.2 can be extended beyond the Stern limit.

### 4.1. Scaling variants

Let us start with the conventional model by scaling the dependent and independent variables as

$$(y^*, z^*, u^*, v^*, w^*, p^*, b^*) = (L, H, U, U, HU/L, NHU, NU) \cdot \mathbf{q}, \tag{27}$$

where $\mathbf{q} = (y, z, u, v, w, p, b)^{\mathrm{T}}$ is a nondimensional column vector. Assuming

$$\sigma^* = \left(\frac{NH}{L}\right)\sigma, \qquad \beta = \frac{2\Omega}{R}, \qquad L = \left(\frac{NH}{\beta}\right)^{1/2}, \qquad L \gg H, \quad N \gg 2\Omega, \tag{28}$$

we can (i), make the traditional approximation by neglecting the Coriolis terms proportional to $2\Omega$ in (1)–(3), and (ii), make the hydrostatic approximation. Note that for typical values of $N$ and $H$ we find a length-scale of a few hundred km and a frequency scale in the order of the earth rotation frequency $\Omega$. For the nondimensional streamfunction we obtain:

$$\psi_{yy} - (\sigma^2 - y^2)\psi_{zz} = 0, \qquad \psi = 0 \quad \text{at } z = 0, 1. \tag{29}$$

In contrast to Stern's model (12) leading to (18), Eq. (29) is of mixed type with turning curves at $y = \pm\sigma$ poleward of which the equation turns elliptic. The boundary value problem is still ill-posed. Nevertheless, for flat boundaries it possesses the well-known smooth solutions in the form of Hermite polynomials. But, as discussed by Maas and Harlander (2007), any additional symmetry breaking of the hyperbolic region – such as for instance due to topography – leads to focusing of characteristics. Therefore, the smooth solutions of the conventional model are extremely sensitive to boundary perturbations. As we will discuss in more detail in Section 4.2, for mixed type boundary value problems internal boundary layers generically occur. Note that (29) cannot be reduced to (18) and thus cannot be solved for more general boundaries.

In contrast to the conventional model, in Section 2.1 we scaled (1)–(5) by

$$(y^*, z^*, u^*, v^*, w^*, p^*, b^*) = (L, \epsilon L, U, U, \epsilon U, 2\Omega\epsilon LU, 2\Omega U\epsilon) \cdot \mathbf{q} \tag{30}$$

and assumed

$$\sigma^* = 2\Omega\epsilon\,\sigma, \qquad \beta = \frac{2\Omega}{R}, \qquad \epsilon = \frac{L}{R} \ll 1, \qquad N^2 \sim (2\Omega\epsilon)^2\sigma. \tag{31}$$

Thus, considering low frequencies and very small $N$ but still keeping the vertical length scale and velocity scale small in comparison with the horizontal scales gives Stern's model (12). As for the conventional scaling, the inertia term can be neglected in the vertical momentum Eq. (3) but the non-traditional Coriolis terms are order one now and have to be kept. Note that in contrast to (29), Stern's model is purely hyperbolic, that is the turning curves of (29) have been mapped to $\pm\infty$.

Physically, the regime considered by Stern may perhaps apply to the deep equatorial ocean, where $N$ is indeed negligible (see e.g. Fig. 2.6 of Tomczak and Godfrey, 1994). The assumption of zonal symmetry is here also acceptable in view of the fact that several observed phenomena in the equatorial ocean are almost zonally symmetric (Ollitrault et al., 2006). To apply Stern's model to atmospheric dynamics three questions need to be addressed: (i) can $N$ become very small in the equatorial atmosphere? (ii) Which upper boundary condition is more realistic for tropospheric inertial waves, wave radiation or wave reflection? (iii) Which role do zonally symmetric waves play for the atmosphere?

(i) As we have already mentioned in the introduction, for equatorial tropospheric motion two distinctly different flow regimes can be identified, a stable one and a convectively mixed one with nearly zero background stratification (Klein, 2003). Stern's model corresponds to the latter if a time-scale much longer than the typical convective time-scale can be justified. It is known (Wheeler and Kiladis, 1999) that equatorial waves can force convection. Our model suggests that inertial waves trapped on a wave attractor might also trigger convection that locally reduces static stability over long periods. (ii) In Appendix B we study the scattering of plane inertial waves at the tropopause. It is found that the tropopause acts as a rigid surface that reflects almost all incoming low-frequency inertial waves. Thus, for inertial waves in a well-mixed neutral troposphere, a wave reflection upper boundary condition appears to be more realistic than a radiation condition. (iii) The study of zonally symmetric modes has a long tradition in atmospheric sciences and such modes have raised interest also recently (Raymond, 2000; Zhao and Takahashi, 2006). In spite of the inhomogeneous distribution of land and sea, zonally elongated patterns of wind and cloud fields are common in the equatorial atmosphere. Thus, for the present conceptual study, zonally averaged solutions might be a worthy first step in the investigation of internal boundary layers in the tropics.

Let us finally study the resilience of the predicted results to stratification and (weak) vertical shear. To do so we add the linear advection term $w^*\bar{u}^*_{z^*}$ to (1) and scale (1)–(5) by

$$(y^*, z^*, u^*, v^*, w^*, p^*, b^*) = (R, R, U, U, U, 2\Omega UR, 2\Omega U) \cdot \mathbf{q} \tag{32}$$

assuming

$$\sigma^* = 2\Omega\,\sigma, \qquad \beta = \frac{2\Omega}{R}, \qquad \bar{u}^*_{z^*} = \alpha^*, \qquad \alpha^* = 2\Omega\,\alpha. \tag{33}$$

Here $\bar{u}^*$ is a dimensional zonal mean flow that depends linearly on $z^*$. For this scaling each term of the nondimensional version of (1)–(5) is of order one. Thus, in contrast to the conventional system and Stern's model, we can neither make the traditional nor the hydrostatic approximation and we have to keep all terms. Using $\alpha' = 1 + \alpha$, $\Gamma = (\alpha' + N^2 - \sigma^2)/\alpha'^2$, $y' = y/\Gamma^{1/2}$, $z' = \alpha' z$ we obtain for the meridional streamfunction:

$$\psi_{y'y'} - (\sigma^2 - \Gamma y'^2)\psi_{z'z'} + 2y'\psi_{y'z'} + \psi'_z = 0, \qquad \psi = 0 \quad \text{at } z' = 0, \alpha'. \tag{34}$$

This equation is strikingly similar to Stern's equation (12). However, for $\Gamma \neq 1$ it cannot be reduced to (18) and thus cannot be solved using the characteristic web method by Maas and Lam (1995). Still, Maas and Harlander (2007) showed that characteristics of (34) converge towards wave attractors which is a first hint for the existence of internal boundary layers. Here we will go one step further and discuss the occurrence of internal boundary layers in numerical solutions.

### 4.2. Finite difference solutions

Hyperbolic or mixed type equations like (12), or (29) and (34) with elliptic boundary conditions are difficult to solve numerically. Usually, standard numerical techniques give inaccurate or even misleading results. Mainly, eigenspectrum degeneracy and the strongly localized character of the solutions accounts for these difficulties. However, with the knowledge of the wave attractor frequency intervals and the gross structure of the expected solution we can apply central finite

differences to obtain (at least qualitative) insight. We use a regular grid and the discretisation:

$$\psi_z \approx \frac{\psi_{k+1,j} - \psi_{k-1,j}}{2\Delta z}, \qquad \psi_{yz} \approx \frac{\psi_{k+1,j+1} - \psi_{k+1,j-1} - \psi_{k-1,j+1} + \psi_{k-1,j-1}}{4\Delta y \Delta z}, \tag{35}$$

$$\psi_{yy} \approx \frac{\psi_{k,j+1} - 2\psi_{k,j} + \psi_{k,j-1}}{\Delta y^2}, \qquad \psi_{zz} \approx \frac{\psi_{k+1,j} - 2\psi_{k,j} + \psi_{k-1,j}}{\Delta z^2} \tag{36}$$

with lateral boundary conditions $\psi = 0$ for $y \to \infty$,[3] $\psi(y, z) = -\psi(-y, z)$ (anti-symmetric modes). Then we solve (12) and (34) as a generalized eigenvalue problem:

$$\mathbf{A}\,\mathbf{V} = \mathbf{B}\,\mathbf{V}\,\mathbf{D} \tag{37}$$

by using the MATLAB routine `eig(A,B)`. Here, **A** and **B** are matrices containing the discretised differential operators, the columns of **V** are the eigenvectors, and the diagonal matrix **D** contains the eigenvalues (frequencies). Note that **B** (corresponding with $\psi_{zz}$) is identical for (12) and (34). Note further that $\Gamma$ in (34) depends on $\sigma$. Therefore, even for $\Gamma$ close to one, the matrices **A** of (12) and (34) differ significantly.

Fig. 5a and b shows two example solutions, one corresponding to (12), the other to (34). Comparing Fig. 5a with Fig. 1b it becomes obvious that the finite difference solution is rather poor. Though not well resolved, the internal shear layer can still be identified in the solution. Most important, however, is the qualitative similarity between Fig. 5a and b. In Fig. 5b we used $\alpha' = 1$ and $N^2 = 9/2$ and still we can find an internal shear layer, though poorly resolved. The figure should be compared with Fig. 4 of Maas and Harlander (2007) that shows the position of the wave attractor for the same $\alpha'$, $\Gamma$, but with $\sigma = 3/2$ instead of the 'eigenfrequency' $\sigma = 1.4996$. It appears that the addition of stability does not remove the shear layers, a result that corresponds with earlier findings (Dintrans et al., 1999). Since the structure of (34) is not changed by introducing a weak shear, there is no reason to believe that vertical shear will remove the internal shear layers. Note that due to the zonal symmetry, critical levels where zonal phase speed equals the zonal mean velocity cannot exist. Nevertheless, $\Gamma$ is singular for $\alpha = -1$, corresponding with a decreasing zonal mean flow with height. For weak shear with $|\alpha| \ll 1$, however, all coefficients of (34) are regular. Note further that, apart from the geometry of the internal shear layer, the solution shown in Fig. 1b depends on the data given in the fundamental intervals. A quantitative comparison of the solutions obtained by the characteristic web method with the solutions obtained via (37) is therefore not useful. In fact, to obtain Fig. 1b we have used boundary conditions that make the hyperbolic boundary value problem well-posed. In contrast, 'well-posedness' seems to be artificially forced by the finite difference approach. A more detailed discussion on the shortcomings of finite difference solutions for ill-posed boundary value problems will be given elsewhere.

Before we give conclusions we note that besides the scalings (27), (30), and (32) discussed above, there exist other scalings that yield intermediate types of equations. For example, changing the coefficient of the mixed derivative term of Stern's Eq. (12) by a positive factor smaller than one turns Stern's boundary value problem from hyperbolic to mixed type. This reminds of the baroclinic Eliassen problem for a forced mean overturning circulation, where the mean vertical shear determines the coefficient in front of the mixed derivative term. Depending on the shear, the

[3] In fact, $\infty$ is replaced by a $y$ that is far enough from the wave attractor.

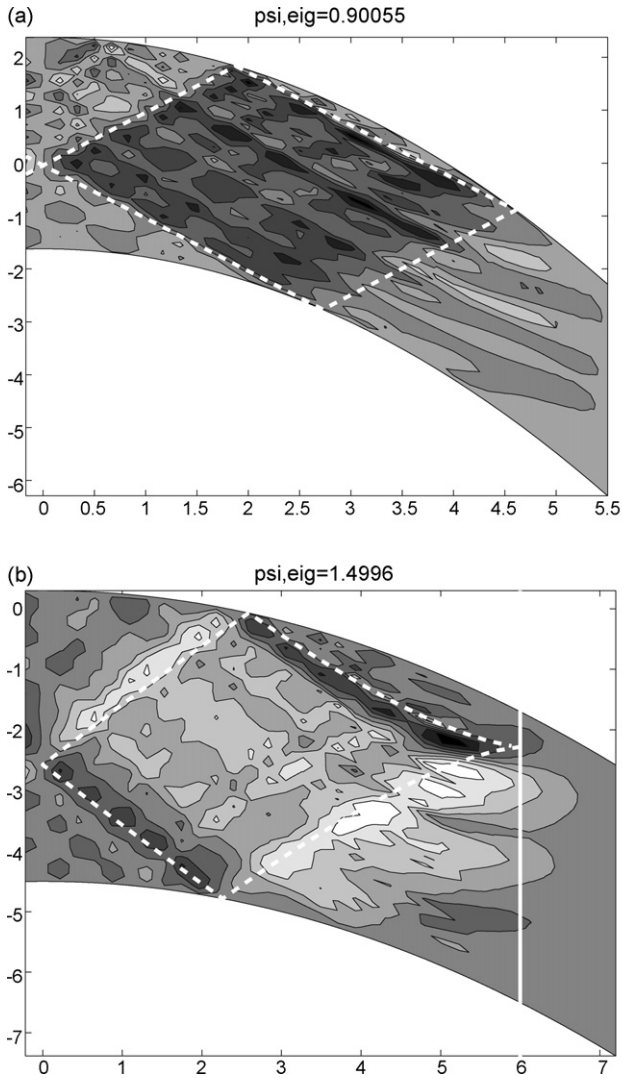


Fig. 5. (a) Numerically computed eigenmode of Stern's model (12) with eigenfrequency $\sigma = 0.90055$. The figure should be compared with Fig. 1. (b) Numerically computed eigenmode of (34) with eigenfrequency $\sigma = 1.4996$. We used $N^2 = 9/2$ and $\alpha' = 1$. Both solutions are computed for a $34 \times 34$ grid and are plotted in the transformed space (16) and (17). Wave attractors are shown by dashed white lines. The turning curve in b) is shown by a solid white line.

problem can be elliptic (in which case an overturning circulation exists) or hyperbolic (in which case modes of inertial instability exist) (Dunkerton, 1989).

## 5. Conclusion

We considered equatorial, zonally symmetric inertial waves, propagating in the meridional plane. Such waves are solutions of the boundary value problem derived by Stern (1963). As was proven by Stewartson (1971, 1972), the solution of Stern's equation possesses singularities in the

velocity field, referred to as internal boundary layers. Nevertheless, a complete understanding of Stern's equation was still lacking since exact solutions that explicitly resolve these singularities were not available. This gap is filled now: we computed exact solutions of Stern's model by using the characteristic web method of Maas and Lam (1995). This relatively new method is suitable to resolve the structure of the *non-viscous* internal boundary layers that contain the attracting limit cycles discussed by Stewartson (1971), to arbitrary fine scales (see Figs. 1b, 2 a and b). Interestingly, a self-similar pattern of shear layers can be found, oriented in alignment with the limit cycles. At its position, the shear layers become infinitely thin. Velocity as well as higher derivatives of the streamfunction blow up within the internal boundary layers and the major part of the kinetic energy of the wave field is trapped there. Similar solutions are discussed by Maas and Lam (1995), Maas et al. (1997), and Manders et al. (2003), but for different geometries and in a different physical context.

Eigensolutions of a viscous (elliptic) version of Stern's boundary value problem can be expected to be symmetrical ($\psi(Y, Z) = \psi(-Y, Z)$) or antisymmetrical ($\psi(Y, Z) = -\psi(-Y, Z)$) with respect to the equator (Rieutord et al., 2002). However, for arbitrary data in the fundamental intervals, Stern's hyperbolic boundary value problem usually possesses *asymmetric* solutions (see for example Fig. 1b). As explained in Appendix A, the reason for the asymmetry is an asymmetric mapping of characteristics into fundamental interval $I_1$ (see Fig. A.1b). To avoid asymmetry, constant data in $I_1$ have to be used. Then an asymmetrical mapping into $I_1$ can no longer affect the solution. One example of this kind was shown in Fig. 3b where we used $f = 0$ in $I_1$, $I_2$, and $I_4$. For this choice of data, a fully trapped antisymmetrical solution can be found. Another example with energy radiation towards mid-latitudes is shown in Fig. 6a. For this Figure we used $\sigma = 0.9$, $f_{I_1} = 0$, $f_{I_2} = \sin(\pi[Y - s_{2,2}]/[s_{2,2} - s_{2,1}])$, and $f_{I_3} = \sin(\pi[Y - s_{3,2}]/[s_{3,2} - s_{3,1}])$ and we plotted $\mathrm{sign}(\psi(Y, Z))$, defining $\mathrm{sign}(0) = 0$. White corresponds to $-1$, dark grey to 1, and light grey to 0. By using constant data in $I_1$, the pattern is antisymmetrical. Note that the asymmetric solutions are generally noncontinuous in contrast to the symmetrical/antisymmetrical solutions. Therefore, it is not possible to obtain the asymmetric solutions by a superposition of a finite number of symmetrical and antisymmetrical solutions.

Stern's equation is relevant for geophysical fluid dynamics since it is an approximation for the equatorial region of a rotating spherical shell (Brown and Stewartson, 1976; Stewartson, 1978). The typical features described here for Stern's boundary value problem can thus be expected also for spherical geometry. For the rotating shell, Stewartson and Rickard (1969) showed that time-harmonic non-viscous solutions are generally singular. Based on numerical computations, Fotheringham and Hollerbach (1998) and Rieutord et al. (2001) discussed the asymptotic properties of inertial modes confined to a spherical shell when viscosity becomes small. They found internal boundary layers similar to the one we discussed for Stern's equation. In contrast to our analysis, the self-similar structure of the boundary layers could not be resolved due to the addition of viscosity, however, it is likely that for the spherical geometry the non-viscous boundary layers possess a fractal structure, too. Rieutord et al. (2001) and Rieutord et al. (2002) showed that viscosity can control the singularities in a rotating spherical shell. They found by numerical and asymptotic techniques that the innermost internal layer scales with $E^{1/3}$, where $E = \nu/2\Omega R^2$ is the Ekman number, $\nu$ is the kinematic viscosity, $\Omega$ is the rotation frequency, and $R$ is the outer radius of the spherical shell. On the other hand, laboratory experiments by Manders and Maas (2004) imply that nonlinear processes might also play a role in determining the width of the boundary layers.

Having noted that internal boundary layers are typical features for waves in rotating spherical shells (and approximations thereof) it might surprise the reader that smooth Rossby-Haurwitz

waves exist for this geometry when the radial component of the motion is small (Longuet-Higgins, 1964). However, as was shown by Stewartson and Rickard (1969) for the spherical shell, the regular expansion that leads to such smooth solutions fails when higher order terms are taken into account, and singular solutions emerge. Thus, paraphrasing Huthnance (1978), these large-scale regular modes continuously leak energy to the fine-scale inertial wave field that is not square-integrable. Inspecting the solutions of Stern's equation from this point of view is instructive. The solution corresponding to $\sigma = 0.37$ (Fig. 4b) reminds of a smooth mode that is cut by the internal boundary layer. There is a spatial scale separation between the region close to the limit cycle and the rest of the domain. This feature is typical for small frequencies. Fig. 6b shows a solution for $\sigma = 0.179$ (in contrast to Fig. 4 we use the cosine for $f_{I_1}$ and minus the cosine for $f_{I_2}$) to underline this fact. Note that the large-scale features of this solution remind us of the pattern of

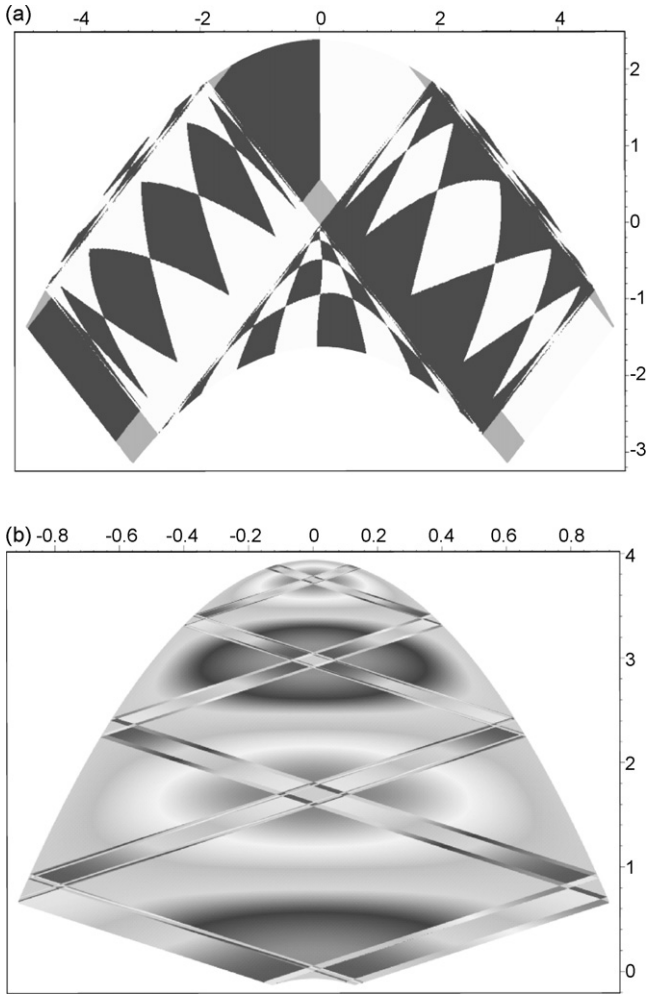


Fig. 6. (a) sign($\psi(Y, Z)$) (defining sign(0) = 0) is plotted for $\sigma = 0.9$ when $f_{I_1} = 0$. The pattern (and the corresponding solution $\psi$) is antisymmetrical. White corresponds to $-1$, dark grey to 1, and light grey to 0. (b) Solution corresponding to $\sigma = 0.179$. Here, cosine functions have been used in the fundamental intervals. See text for more details.

deep equatorial currents recently observed in the Eastern Equatorial Atlantic Ocean (Bourlés et al., 2003).

Numerical techniques or severe truncations of perturbation series might artificially regularize local singularities (Huthnance, 1978; Swart et al., 2007) and such approaches should therefore be applied with caution to hyperbolic boundary value problems. Thuburn et al. (2002) for instance look for time-harmonic solutions of a non-viscous, non-hydrostatic, compressible fluid comprised in a rotating spherical shell. As Stern's equation, this problem is ill-posed and regular eigenmodes cannot be expected (Stewartson and Rickard, 1969; Brown and Stewartson, 1976; Stewartson, 1978; Dintrans et al., 1999). Surprisingly, Thuburn et al. discuss only regular solutions found by a numerical finite difference approach. To understand better how solutions with internal boundary layers are represented in finite difference models we solved Stern's Eq. (12) as a generalized eigenvalue problem by using central finite differences. We found that even with low resolution a regularized internal boundary layer is visible (compare the right hand side of Fig. 1b with Fig. 5a). We then extended Stern's equation by adding stratification and vertical shear. For this model we found regularized versions of the boundary layers in finite difference solutions, too. Thus it appears that the boundary layers found for Stern's boundary value problem are resilient to small amounts of vertical shear and stratification. This implies that the results discussed in Section 3.2 hold beyond the Stern limit of a homogeneous fluid.

Taking together our results and what has been published before on internal wave solutions of fluids confined to (semi-)closed domains it is evident that solutions with internal boundary layers are relevant to geophysical fluid dynamics. Stronger, for the non-viscous case, smooth eigenmodes appear to be exceptional, occurring for special geometries only, or being the result of approximations, resulting for example through the exclusion of vertical motions or the assumption of quasi-geostrophy. The question arises if the type of internal boundary layer discussed here has been observed in the atmosphere or the oceans. Of course, it would be too optimistic to expect that clean boundary layers, as shown in the Figs. 1, 3, 4 and, can be observed. Nevertheless, effects of internal boundary layers might be observable in certain regions. From laboratory experiments (Maas, 2001) it is known that the strongest mixing occurs around points where the internal boundary layers focus at the boundaries. If we consider the equatorial tropopause as the upper boundary, tropospheric air could effectively be mixed into the tropopause at those points. This kind of mixing could work in addition to convective overshooting (Sherwood and Dessler, 2003), where air from the tropospheric boundary layer is lifted into the tropopause. We conclude by saying that internal boundary layers might be an issue in deep ocean mixing or stratosphere–troposphere coupling (Shepherd, 2002) that should possibly be taken into account when observations of equatorial deep currents or troposphere–stratosphere air exchange are interpreted.

## Acknowledgments

We thank M.T. Montgomery, T.J. Dunkerton, and an anonymous reviewer for helpful comments that improved the paper. We also thank F. Eijgenraam for help with the numerical programs. U.H. was supported by the Netherlands Organization for Scientific Research (N.W.O) under grant 813.03.004 (ALW3PJ/03-23).

## Appendix A. How can fundamental intervals be found?

In general, the so called grazing points can be used to construct the fundamental intervals. At grazing points, the boundary slope equals the slope of the characteristics. For a domain bounded

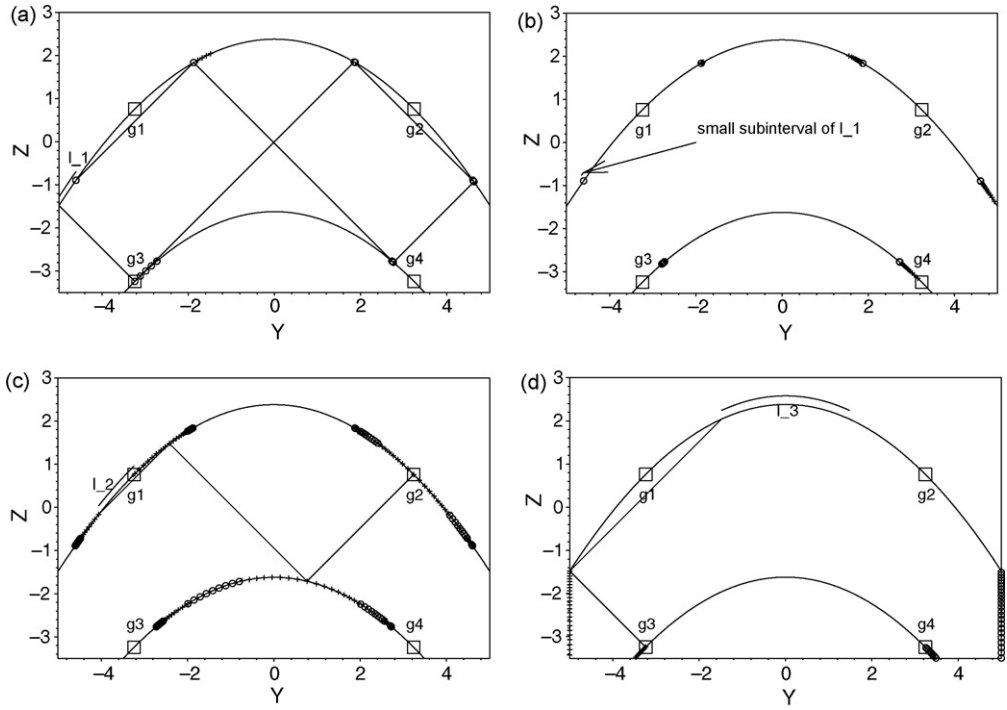


Fig. A.1. Construction of fundamental intervals for $\sigma = 0.9$ in the $Y$–$Z$-frame. Circles (crosses) denote reflection points of a characteristic web from the boundaries when a $c^+$ ($c^-$) characteristic is 'launched' from a fundamental interval. The boxes indicate the position of the grazing points $g_1, \ldots, g_4$. Fundamental intervals are denoted by $I_1, \ldots, I_3$ and are shown by line segments above the upper parabolic boundary. The polygons in between the two boundaries are the characteristic webs used to find the fundamental intervals. In (a) characteristics are launched from $I_1$ having a distance of $\Delta Y = 0.1$. In (b) characteristics are started from a small subinterval of $I_1$ ($\Delta Y = 0.002$). In (c) and (d) characteristics from $I_2$ and $I_3$ ($\Delta Y = 0.1$) are mapped to the boundaries.

by a polygon, for example, grazing points correspond with corner points of the polygon (Maas et al., 1997). For the equatorial shell geometry, four grazing points exist and they correspond to points where the boundary slope is one. These points are shown in Fig. A.1 by squares and are denoted by $g_i, i = 1, \ldots, 4$. Typically, grazing points divide the boundaries into regions with different reflection properties: a characteristic hitting the boundary to the left of a grazing point will be reflected in the opposite direction than a characteristic hitting the boundary to the right of a grazing point.

Let us now construct the fundamental intervals for waves with frequency $\sigma = 0.9$. (For other frequencies the construction is similar as is shown in Table A.1). To make the discussion tighter we introduce the notation $g_i \| c^+, k \| s_{j,n}$ that has to be read in the following way: launch a $c^+$ characteristic from $g_i$, follow it along $k$ reflections, and read off the final reflection point $s_{j,n}$, corresponding to the lower bound ($n = 1$) or to the upper bound ($n = 2$) of fundamental interval $j$. Note that fundamental intervals are located at the top of the equatorial shell and that we specify their boundaries by $Y$ values alone.

To find the first fundamental interval $I_1$, the following two operations have to be carried out

$$g_3 \| c^-, 1 \| s_{1,1}, \quad \text{and} \quad g_3 \| c^+, 5 \| s_{1,2}.$$

Table A.1
A summary of all characteristic webs used to find the fundamental intervals

| $\sigma$ | 0.9 | 0.52 | 0.37 | 0.179 |
|---|---|---|---|---|
| $s_{1,1}$ | $g_3 \| c^-, 1 \| s_{1,1}$ | $g_3 \| c^-, 1 \| s_{1,1}$ | $-1.7402$ | $g_3 \| c^-, 1 \| s_{1,1}$ |
| $s_{1,2}$ | $g_3 \| c^+, 5 \| s_{1,2}$ | $g_3 \| c^+, 3 \| s_{1,2}$ | $s_{1,1} \| c^-, 10 \| s_{1,2}$ | $g_3 \| c^+, 17 \| s_{1,2}$ |
| $s_{2,1}$ | $g_2 \| c^+, 3 \| s_{2,1}$ | $g_1$ | $g_3 \| c^-, 4 \| s_{2,1}$ | $g_3 \| c^-, 8 \| s_{2,1}$ |
| $s_{2,2}$ | $g_1$ | $g_4 \| c^-, 2 \| s_{2,2}$ | $g_4 \| c^+, 2 \| s_{2,2}$ | $g_4 \| c^+, 2 \| s_{2,2}$ |
| $s_{3,1}$ | $g_3 \| c^-, 2 \| s_{3,1}$ | 0 | $g_1 \| c^-, 10 \| s_{3,1}$ | $g_1 \| c^-, 18 \| s_{3,1}$ |
| $s_{3,2}$ | $-s_{3,1}$ | $s_{3,1} \| c^+, 4 \| s_{3,2}$ | $g_1$ | $g_1$ |
| $s_{4,1}$ | – | $g_3 \| c^-, 2 \| s_{4,1}$ | – | – |
| $s_{4,2}$ | – | $g_2$ | – | – |

Graphically, these operations are shown in Fig. A.1a. As mentioned above, the boundaries $s_{1,1}$ and $s_{1,2}$ of $I_1$ are $Y$-values, that is the interval has to be read off 'vertically' from the figure, which is shown in the $Y$–$Z$-frame. Note that, following the characteristic web, $s_{1,2}$ is the reflection point at the upper boundary which comes closest to $s_{1,1}$. We can check whether or not $I_1$ is a first fundamental interval by 'launching' characteristics from this interval and verify that none of those will enter the interval again. The circles (crosses) in Fig. A.1 show boundary reflection points of a characteristic web when a $c^-$ ($c^+$) characteristic is launched from $I_1$ (60 reflections are computed for each characteristic). Indeed, no characteristic is mapped back onto $I_1$.[4]

Fig. A.1b demonstrates that relatively large boundary segments can be mapped onto very small parts of the fundamental interval. This is caused by the small distance between the upper bound of $I_1$ and the limit cycle, combined with a fast focusing rate. Note that in contrast to Fig. A.1a, the set of characteristics launched from the small subinterval (it covers only 11% of $I_1$) is rather dense ($\Delta Y = 0.002$).

To find the second fundamental interval $I_2$ we perform (see Fig. A.1c):

$$g_2 \| c^+, 3 \| s_{2,1}.$$

As upper bound of $I_2$ we take $g_1$. Note that for the chosen characteristic web, $s_{2,1}$ is that reflection point at the upper boundary which comes closest to $g_1$. Therefore, $I_2$ is a possible fundamental interval. This can be tested by mapping points from $I_2$ onto the boundary to verify that no characteristic is mapped back onto $I_1$ or $I_2$. Finally, a third fundamental interval is necessary corresponding to characteristics 'escaping' to infinity. Obviously, $c^-$ characteristics which intersects with a point located beyond $g_3$ (i.e. further away from the equator than $g_3$) cannot be mapped back into the equatorial region. Therefore, we apply

$$g_3 \| c^-, 2 \| s_{3,1},$$

to find the lower bound of $I_3$ (see Fig. A.1d). The upper bound is located symmetrically to the right of the $Z$-axis. As for the other fundamental intervals we can verify whether the data in $I_3$ are independent from $I_1$ and $I_2$. Note that for computational reasons we have introduced vertical walls at $Y_w = \pm 5.1$, visible in Fig. A.1d. These walls do not affect the fundamental intervals as long as $|Y_w|$ is larger as the magnitude of the lower bound of $I_1$.

[4] One circle seems to be in the fundamental interval. However, the interval displayed in the figure has to be projected vertically on the upper boundary. Then it becomes plausible that the suspicious point is in fact located outside of the interval.

A synopsis of Fig. A.1a–d shows that the boundary is completely covered by reflection points (crosses or circles). Clearly, a one-to-one correspondence between the boundary points outside and inside the fundamental intervals exists. Since any point inside the fluid domain can be mapped to a point on the boundary by a $c^+$ or a $c^-$ characteristic, the solution of (18) is given uniquely if $f$ is specified in the fundamental intervals only. This forms the basis of the characteristic web method introduced by Maas and Lam (1995). The algorithm to find $\psi$ at any point $P$ inside the fluid domain can be summarized as follows:

(i) Launch a $c^+$ characteristic at $P$ and trace it back until it intersects with one of the fundamental intervals. Read off the value of $f = f^+$.
(ii) Repeat point (i) but with a $c^-$ characteristic. This gives $f = f^-$.
(iii) Find the streamfunction at $P$ by $\psi(P) = f^- - f^+$.

### A.1. Interhemispheric asymmetry

A conclusion we can draw from (i) to (iii) in combination with Fig. A.1b and d is that, for arbitrary data in the fundamental intervals, solutions of Stern's equation will in general show interhemispheric asymmetry. To see this we consider an area $S$ in the fluid, defined by points which can be mapped by a single $c^-$ characteristic onto $I_1$ and by a single $c^+$ characteristic onto $I_3$. The streamfunction for all points $P$ of $S$ is simply given by $\psi(P) = f^-_{I_1} - f^+_{I_3}$, where $f^\pm_{I_{1,3}}$ stands for the $f$-value of the characteristic starting at $P$ and intersecting with the fundamental interval $I_{1,3}$. Next consider the area $S'$ which is the mirror domain of $S$ with respect to the $Z$-axis. Clearly, all points of $S'$ can be mapped by a single $c^-$ characteristic onto $I_3$. However, as is obvious from Fig. A.1b, almost all points of $S'$ can be mapped onto the small subinterval of $I_1$ shown in the figure. Consequently, $\psi(P')$ generally differs from $-\psi(P)$, that is we cannot expect symmetric (or anti-symmetric) solutions for the equatorial shell if the data in $I_1$ vary with $Y$.

### A.2. Number of fundamental intervals

Let us address the question of how many fundamental intervals we can expect for a certain frequency. For the convex geometries considered by Maas and Lam (1995) and Manders et al. (2003) the results suggest that $N$ limit cycles imply $N + 1$ fundamental intervals. For the Stern equation, characteristics can additionally be mapped to $\pm\infty$, so we expect more than $N + 1$ fundamental intervals. It turns out that for Stern's equation $N + 2$ fundamental intervals exist. Note that, even if no counter example of this rule has been found yet, it is not mathematically proven. Therefore, the rule has to be used with caution.

### A.3. Summary

Table A.1 gives all the characteristic webs used to determine fundamental intervals at the upper boundaries of the equatorial shell for four different frequencies. The symbol $g_i \| c^+, k \| s_{j,n}$ means that a $c^+$ characteristic has to be launched from $g_i$ and followed along $k$ reflections, to find one of the two boundaries of a fundamental interval. Here $s_{j,n}$ denotes the $Y$-value of the lower bound ($n = 1$) or the upper bound ($n = 2$) of fundamental interval $j$, located at the upper boundary. Note that the choice of fundamental intervals for a given frequency is not unique. In other words, one can use different characteristic webs to find a fundamental interval. For example, for $\sigma = 0.9, 0.52, 0.179$ we used $g_3$ as starting point for the characteristics to find $I_1$.

In contrast, for $\sigma = 0.37$ we launched a $c^-$-characteristic at $(Y, Z_s(Y))$ with $Y = -1.7402$ to find an appropriate $I_1$. The interval is smaller compared with the other fundamental intervals $I_1$, but it is still located to the left of the point where the wave attractor touches the upper boundary. The position of the internal boundary layer is independent of the choice of fundamental intervals, nevertheless, the solution (i.e. the streamfunction) depends on this choice and, of course, on the data specified in the intervals.

## Appendix B. Internal wave reflection

If atmospheric waves (internal and planetary) would propagate into the mesosphere without any back scatter, refraction, or breaking, an atmospheric corona would be produced as was pointed out by Charney and Drazin (1961) [see Hines (1989) for a retrospective view on atmospheric gravity waves]. Today we know that only some fraction of the wave energy which is radiated upward from the earth's surface can actually reach the middle atmosphere. To estimate the ratio between transmitted and reflected waves at the troposphere–stratosphere interface let us consider the region below the tropopause as well-mixed with constant Brunt-Väsälä frequency $N_1^2 = 0$, and the lower part of the tropopause as a region with constant $N_2^2 = 7 \times 10^{-4}\,\mathrm{s}^{-2}$. The number for $N_2$ comes from a recent study on the sharpness of the troposphere–tropopause boundary (Birner et al., 2002), showing that the transition is much sharper than expected from earlier estimates. We assume further that the atmosphere is at rest, that there is no density jump at the tropopause, and that the Boussinesq-approximation holds. For simplicity, we also neglect the beta effect. This is justified by the fact that Rossby waves cannot transport energy vertically in a homogeneous medium. The beta effect modifies the inertial wave propagation. However, this modification does not essentially change the results presented in the following.

With the assumptions above we obtain from (1)–(5) for a zonally symmetric well-mixed troposphere:

$$\psi_{zz} - \left(\frac{4\Omega^2 - \sigma^2}{\sigma^2}\right)\psi_{yy} = 0, \tag{B.1}$$

where $v = -\psi_z$ and $w = \psi_y$. Note that in (12) we neglected inertia in the vertical momentum equation. Then the coefficient in (B.1) would reduce to $4\Omega^2/\sigma^2$. However, keeping or neglecting this term does not change the main results given below.

In the layer representing the tropopause, $N_2^2 \gg 4\Omega^2$, thus we can neglect the non-traditional terms there. Eqs. (1)–(5) yield:

$$\psi_{zz} - \left(\frac{N_2^2 - \sigma^2}{\sigma^2}\right)\psi_{yy} = 0. \tag{B.2}$$

To find the reflection and transition coefficients, we consider plane waves with an upward group velocity, having amplitude one, and impact angle $\theta = \arctan(n_i/l_i)$, where $l_i$ and $n_i$ are the incident meridional and vertical wavenumbers (see Fig. B.1a). Note that group velocity stands perpendicular to the wavenumber vector. At the troposphere–tropopause interface the matching conditions are $w_1 = w_2$ and $p_1 = p_2$, where $w_1$, $w_2$, $p_1$, $p_2$ stand for the vertical velocity and pressure in the troposphere (index 1) and in the tropopause (index 2). From these conditions we find:

$$T = \frac{2n_i}{(n_i + n_t)}, \qquad R = T - 1 \tag{B.3}$$

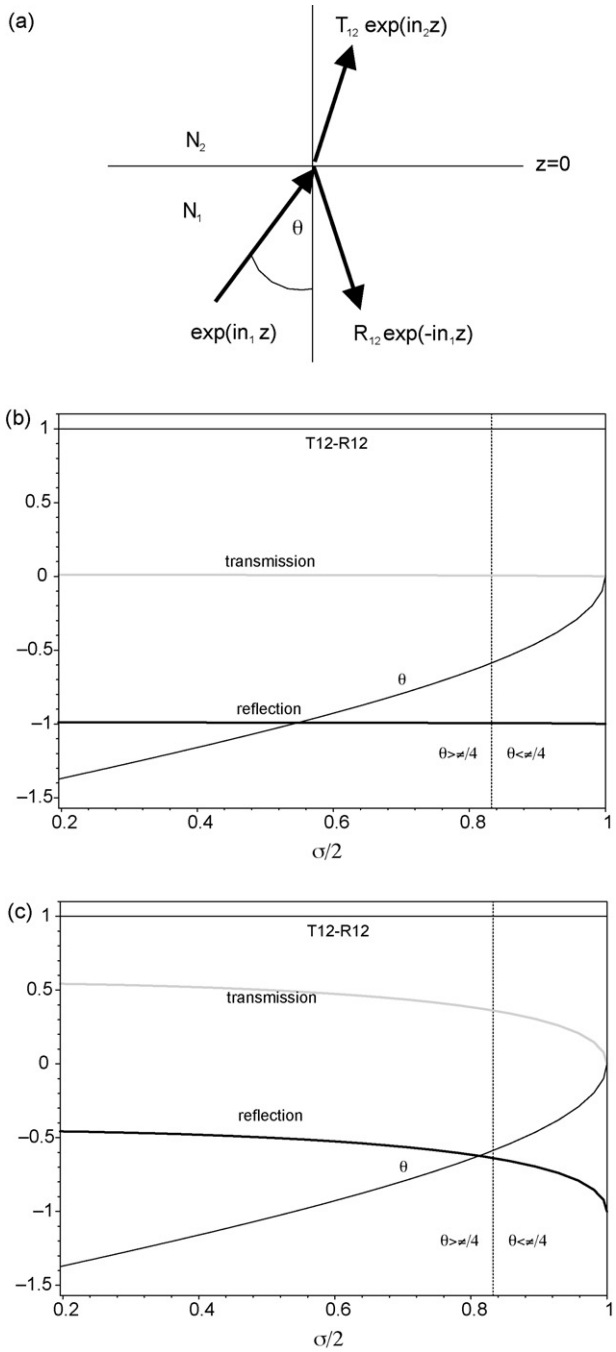


Fig. B.1. (a) An upward propagating internal wave with vertical wavenumber $n_1$ is partly reflected and partly transmitted at the lower boundary of the tropopause at $z = 0$. (b) Transmission and reflection coefficients as a function of frequency. We used $\Omega = 7.2 \times 10^{-5}\,\mathrm{s}^{-1}$, $N_1^2 = 0$ and $N_2^2 = 7 \times 10^{-4}\,\mathrm{s}^{-2}$. Note that $T_{12} - R_{12} = 1$. The thin curve shows the angle of incidence $\theta$, as defined in (a). To the right of the vertical dotted line, $\theta$ is smaller than 45° (steep ray), to the left it is larger (shallow ray). In (c) we used $N_1^2 = 0$ and $N_2^2 = 7(2\Omega)^2$.

with

$$n_t^2 = \left(\frac{N_2^2}{\sigma^2 - 1}\right) l_i^2 \quad \text{and} \quad \sigma^2 = \frac{4\Omega^2 l_i^2}{(n_i^2 + l_i^2)}. \tag{B.4}$$

Fig. B.1b shows the inertial wave reflection and transmission coefficients as a function of the normalized frequency. Due to the fact that the vertical motion is not hampered by stratification in the well-mixed lower layer but suppressed in the strongly stratified upper layer, the reflection of inertial waves is almost elastic. No internal gravity waves can be excited by inertial waves at the interface. In spite of the simplicity of the reflection process described, we can say that an upward traveling inertial wave field will be reflected almost completely at the tropopause. Subsequently, it propagates downward into the troposphere where it might be reflected a second time at the earth's surface and so forth.

It is instructive to reduce $N_2^2$ to see for which value transmission becomes visible. Fig. B.1c shows $T$ and $R$ for $N_1^2 = 0$ and $N_2^2 = 7(2\,\Omega)^2$. Interestingly, even for such a weak stratification, reflection is rather prominent.

Finally, let us compare the results with the reflection of internal gravity waves when the troposphere is not well-mixed. For such a more classical situation, the formulas for the reflection and transmission coefficients can be found in Tolstoy (1973). With the assumption made above (no density jump at the interface, Boussinesq approximation), the general formulas given by Tolstoy reduce to (B.3) and (B.4) but with $\sigma^2 = N_1^2 l_i^2/(n_i^2 + l_i^2)$. For a typically tropospheric stability of $N_1^2 = 1 \times 10^{-4}\,\mathrm{s}^{-2}$ and $N_2^2 = 7 \times 10^{-4}\,\mathrm{s}^{-2}$, the transmission and reflection coefficients (when plotted against $\sigma/N_1$) are exactly the same as the one shown in Fig. B.1c. Remarkably, for all impact angles (shown by the thin curve), the magnitude of $R$ is roughly 0.5 or larger (see Fig. B.1d). We see that for a stratified troposphere too, the tropopause is a rather effective reflector for internal gravity waves.

## References


Birner, T., Dörnbrack, A., Schumann, U., 2002. How sharp is the Tropopause in midlatitudes? Geophys. Res. Lett. 29, 10.1029/2002GL015142.

Bourlés, B., Andrié, C., Gouriou, Y., Eldin, G., DuPenhoat, Y., Freudenthal, S., Dewitte, B., Gallois, F., Chuchla, R., Baurand, F., Aman, A., Kouadio, G., 2003. The deep currents in the Eastern Equatorial Atlantic Ocean. Geophys. Res. Lett. 30 (5), 8002.

Bretherton, F.P., 1964. Low frequency oscillations trapped near the equator. Tellus 16, 181–185.

Brown, S.N., Stewartson, K., 1976. Asymptotic methods in the theory of rotating fluids. In: O'Malley, R.E. (Ed.), Asymptotic Methods and Singular Perturbations. SIAM-AMS Proceedings, vol. 10, American Mathematical Society, pp. 1–21.

Charney, J.G., 1963. A note on large-scale motions in the tropics. J. Atmos. Sci. 20, 607–609.

Charney, J.G., Drazin, P., 1961. Propagation of planetary-scale disturbances from the lower into the upper atmosphere. J. Geophys. Res. 66, 83–109.

Colin de Verdière, A., Schopp, R., 1994. Flows in a rotating spherical shell: the equatorial case. J. Fluid Mech. 276, 233–260.

Dintrans, B., Rieutord, M., Valdettaro, L., 1999. Gravito-inertial waves in a rotating stratified sphere or spherical shell. J. Fluid Mech. 398, 271–297.

Dunkerton, T.J., 1989. Nonlinear Hadley circulation driven by asymmetric differential heating. J. Atmos. Sci. 46, 956–974.

Fotheringham, P., Hollerbach, R., 1998. Inertial oscillations in a spherical shell. Geophys. Astrophys. Fluid Dynam. 89, 23–43.

Gerkema, T., Shrira, V.I., 2005. Near-inertial waves on the 'non-traditional' $\beta$ plane. J. Geophys. Res. 110, C01003.

Harlander, U., Maas, L.R.M., 2006. Characteristics and energy rays of equatorially trapped, zonally symmetric internal waves. Meteorol. Zeitschrift 15, 439–450.

Hendershott, M.C., 1981. Long waves and ocean tides. In: Warren, B.A., Wunsch, C. (Eds.), Evolution of Physical Oceanography. MIT Press, Cambridge, MA, pp. 292–341.
Hines, C.O., 1989. Earlier days of gravity waves revisted. PAGEOPH 130, 151–170.
Hollerbach, R., Kerswell, R.R., 1995. Oscillatory internal shear layers in rotating and precessing flows. J. Fluid Mech. 298, 327–339.
Huthnance, J.M., 1978. Inertial waves and an initial-value problem for a thin spherical rotating fluid shell. J. Fluid Mech. 86, 273–288.
Israeli, M., 1972. On trapped oscillations of rotating fluids in spherical shells. Stud. Appl. Maths L1, 219–237.
Kerswell, R.R., 1995. On the internal shear layers spawned by the critical regions in oscillatory Ekman boundary layers. J. Fluid Mech. 298, 311–325.
Klein, R., 2003. An applied mathematical view of meteorological modeling. In: J.M. Hill, R. Moore (Eds.), Proceedings of the ICIAM, Sydney, Australia, pp. 1–44.
LeVeque, R.J., 2002. Finite Volume Methods for Hyperbolic Problems. Cambridge University Press.
Longuet-Higgins, M.S., 1964. Planetary waves on a rotating sphere. Proc. R. Soc. A 279, 446–473.
Maas, L.R.M., 2001. Wave focusing and ensuing mean flow due to symmetry breaking in rotating fluids. J. Fluid Mech. 437, 13–28.
Maas, L.R.M., 2005. Wave attractors: linear yet nonlinear. Int. J. Bifurcation Chaos 15, 2757–2782.
Maas, L.R.M., Benielli, D., Sommeria, J., Lam, F.-P.A., 1997. Observation of an internal wave attractor in a confined, stable stratified fluid. Nature 388, 557–561.
Maas, L.R.M., Harlander, U., 2007. Equatorial wave attractors and inertial oscillations. J. Fluid Mech. 570, 47–67.
Maas, L.R.M., Lam, F.-P.A., 1995. Geometric focusing of internal waves. J. Fluid Mech. 300, 1–41.
Majda, A., Klein, R., 2003. Systematic multi-scale models for the tropics. J. Atmos. Sci. 60, 393–408.
Manders, A.M.M., Duistermaat, J.J., Maas, L.R.M., 2003. Wave attractors in a smooth convex enclosed geometry. Physica D 186, 109–132.
Manders, A.M.M., Maas, L.R.M., 2003. Observations of inertial waves in a rectangular basin with one sloping boundary. J. Fluid Mech. 493, 59–88.
Manders, A.M.M., Maas, L.R.M., 2004. On the three-dimensional structure of the inertial wave field in a rectangular basin with one sloping boundary. Fluid Dynam. Res. 35, 1–21.
Myint-U, T., 1987. Partial Differential Equations for Scientists and Engineers, 3rd ed. North Holland, New York.
Ogilvie, G.I., Lin, D.N.C., 2004. Tidal dissipation in rotating giant planets. Astrophys. J. 610, 477–509.
Ogura, Y., Phillips, N.A., 1962. Scale analysis of deep moist convection and some related numerical calculations. J. Atmos. Sci. 19, 173–179.
Ollitrault, M., Lankhorst, M., Fratantoni, D., Richardson, P., Zenk, W., 2006. Zonal intermediate currents in the equatorial Atlantic Ocean. Geophys. Res. Lett. 33, 05605.
Pichler, H., 1986. Dynamik der Atmosphäre. BI-Wissenschaftsverlag.
Raymond, W.H., 2000. Equatorial meridional flows: rotationally induced circulations. Pure Appl. Geophys. 157, 1767–1779.
Rieutord, M., Georgeot, B., Valdettaro, L., 2001. Inertial waves in a rotating spherical shell: attractors and asymptotic spectrum. J. Fluid Mech. 435, 103–144.
Rieutord, M., Valdettaro, L., Georgeot, B., 2002. Analysis of singular inertial modes in a spherical shell: the slender toroidal shell model. J. Fluid Mech. 463, 345–360.
Shepherd, T.G., 2002. Issues in stratosphere–troposphere coupling. J. Met. Soc. Jpn. 80, 769–792.
Sherwood, S.C., Dessler, A.E., 2003. On the control of stratospheric humidity. Geophys. Res. Lett. 27, 2513–2516.
Stern, M.E., 1963. Trapping of low frequency oscillations in an equatorial 'boundary layer'. Tellus 15, 246–250.
Stewartson, K., 1971. On trapped oscillations of a rotating fluid in a thin spherical shell. Tellus 23, 506–510.
Stewartson, K., 1972. On trapped oscillations of a rotating fluid in a thin spherical shell II. Tellus 24, 283–287.
Stewartson, K., 1978. Waves in homogeneous fluids. In: Roberts, P.H., Soward, A.M. (Eds.), Rotating Fluids in Geophysics. Academic Press, pp. 67–103.
Stewartson, K., Rickard, J.A., 1969. Pathological oscillations of a rotating fluid. J. Fluid Mech. 5, 577–592.
Stewartson, K., Walton, I.C., 1976. On inertial oscillations in the oceans. Tellus 28, 71–73.
Swart, A., Sleijpen, G.L.G., Maas, L.R.M., Brandts, J., 2007. Numerical solution of the two dimensional Poincaré equation. J. Comput. Appl. Math. 200, 317–341.
Thuburn, J., Wood, N., Staniforth, A., 2002. Normal modes of deep atmospheres. I. Spherical geometry. Q. J. R. Meteorol. Soc. 128, 1771–1792.
Tilgner, A., 1999. Driven inertial oscillations in spherical shells. Phys. Rev. E 59, 1789–1794.
Tolstoy, I., 1973. Wave Propagation. McGraw-Hill, Inc., New York.

Tomczak, M., Godfrey, J.S., 1994. Regional Oceanography: An Intoduction. Pergamon.

Vlasenko, V., Stashchuk, N., Hutter, K., 2005. Baroclinic Tides. Cambridge University Press.

Wheeler, M., Kiladis, G.N., 1999. Convectively coupled equatorial waves: analysis of clouds and temperature in the wavenumber-frequency domain. J. Atmos. Sci. 56, 374–399.

Zhao, N., Takahashi, M., 2006. Zonally symmetric normal modes associated with the AO/NAM under a seasonally varying background climatology. Tellus 58A, 575–583.